Polymer Chemistry

ROYAL SOCIETY OF CHEMISTRY

PAPER

View Article Online
View Journal | View Issue

Cite this: *Polym. Chem.*, 2025, **16**, 5106

Structure and dynamics in poly(ethylene oxide)-blended single-ion conducting polymer electrolytes based on side-chain ionomers

Govinda Prasad Devkota, Carter K. Dauenhauer, Jizhou Jiang and Jennifer L. Schaefer *

While single-ion conducting polymer electrolytes (SICPEs) are highly promising candidates for safer polymer electrolytes due to their stability and high transference number, their practical application is often hindered by substantially lower ionic conductivities. In this study, we investigate morphology and dynamics of a family of SICPEs based on a side-chain ionomer blended with poly(ethylene oxide) (PEO) at various ratios. In the pure state, the side-chain ionomer is liquid crystalline with dense ionic layers. PEO addition reduced the primary glass transition temperature, accompanied by the emergence of a new glass transition attributed to the ionomer's polystyrene backbone. Morphologically, blends with lower PEO content maintained the lamellar structure of the pure ionomer, while higher PEO ratios resulted in increased disorder. The ionic conductivity of the blend at high PEO content (EO–Li ratio of 20–1) reached 7.9 × 10^{-5} S cm^{-1} at 90 °C, approximately four orders of magnitude greater than that of pure ionomer and similar to that of other PEO-ionomer blends containing tethered –sulfonyl(trifluoromethylsulfonyl)imide (–$TFSI^-$) anions. Dielectric spectroscopy revealed that PEO addition leads to increased coupling between dielectric relaxation and long-range ion transport.

Received 1st August 2025,
Accepted 14th November 2025

DOI: 10.1039/d5py00769k

rsc.li/polymers

Introduction

Solid polymer electrolytes (SPEs) are researched as next-generation alternatives, potentially improving rechargeable battery safety by eliminating flammable organic liquid components. Their tunable mechanical properties, low cost processing, wide electrochemical stability windows, improved thermal stability, and lower density compared to inorganic counterparts make them viable candidates for all solid-state batteries.[1–3] However, the traditional SPEs, particularly those based on poly(ethylene oxide) (PEO), have low ionic conductivity at room temperature and low cation transference number, which collectively limit their practical applications.[4–8]

Single-ion conducting polymer electrolytes (SICPEs), a particular class of the polymer electrolytes, are of great interest due to their high transference number.[9] By covalently attaching the anionic site to the polymer framework, SICPEs theoretically achieve a cation transference number approaching unity.[9–11] High active ion transference number results in higher limiting current and mitigated dendrite growth from metal anodes if active ion conductivity is maintained.[12] However, despite these key advantages, SICPEs suffer from substantially lower ionic conductivity than dual-ion conductors.

A fundamental challenge in many polymer electrolytes is that ionic transport is strongly coupled with the segmental dynamics of the polymer backbone. This phenomenon is observed in polymer electrolytes containing polar functional groups, including the most commonly investigated poly(ethylene oxide) (PEO), poly(carbonates), poly(esters), and others.[13–18] This coupling often results in low ionic conductivities, especially at ambient temperatures, as ionic mobility is constrained by sluggish motion of the polymer backbone, preventing achieving comparable conductivities to liquid electrolytes. To overcome this, particularly in SICPEs, a key research focus has been on designing new SICPEs with decoupled ion transport from the polymer backbone dynamics.

One potential approach for achieving decoupling is ion transport through dense ionic aggregates. Several ionomers with precise and near-precise tethered ion spacing on the main chain polymer backbone or directly pendant to the backbone have been shown to contain percolated ion clusters, a necessary condition for ion transport predominantly through the ionic aggregate to result in high bulk ionic conductivity.[19–22] Still, small changes to the molecular structure of these ionomers can impact the ion cluster morphology

Department of Chemical and Biomolecular Engineering, University of Notre Dame, Notre Dame, Indiana 46556, USA. E-mail: Jennifer.L.Schaefer.43@nd.edu

and no real system of this type that lacks additional solvation sites (small-molecule solvents or polymers) or supporting ions has been shown to facilitate lithium-ion transport at a rate that rivals that of SICPEs containing polar chains.

To further advance this strategy of ion transport through ion clusters, our previous work focused on designing SICPEs with ionic sites strategically positioned on flexible, non-polar side-chains of the nonpolar polymer backbone.[23–25] This architecture promotes nanoscale phase segregation and the self-assembly of ordered ionic domains. Side-chain ionomers with *para*(polyphenylene) backbones and alkyl side-chains with varying lengths (C6 to C15) terminated with lithium titrated –sulfonyl(trifluoromethylsulfonyl)imide (–TFSI$^-$) anions were found to self-assemble predominately with one-dimensional ionic domains,[24] whereas a side-chain ionomer termed LiPSC10TFSI with more flexible poly(styrene) backbone and decyl side-chains terminated with the same ionic group was found to self-assemble with two-dimensional (lamellar) ionic domains over a wide temperature range (from the ambient temperature glassy state to above 180 °C).[25] These SICPEs can be classified as liquid crystalline at temperatures above their glass transition and exhibit elevated ionic conductivity in their pure state, lacking small-molecule or polymeric solvent, when compared with other dry, non-solvating ionomers such as LiPSTFSI.[26] However, their ionic conductivity is still lower than necessary as a battery electrolyte for many applications – generally an active ion conductivity of at least 10^{-4} S cm^{-1} at the operating temperature is sought – and even lower than polyether-containing single-ion conductors.[27]

In other recent literature, it has been shown that swelling of ionic aggregates with solvating groups can enhance ionic conductivity.[27] We hypothesized that the stable morphology of the liquid crystalline LiPSC10TFSI made it an ideal candidate to investigate the impact of doping the ionic clusters with a solvating polymer, effectively increasing the number of lithium solvation sites in the ionic domain. Here, we report on the thermal properties, morphology, and ion transport properties of blends of LiPSC10TFSI prepared *via* scalable free-radical polymerization with poly(ethylene oxide) (PEO), varying the ethylene oxide (EO) to lithium (Li) ratios in the range of EO–Li of 2–1 to 20–1. We find that inclusion of PEO has profound implications on all investigated properties, including mesoscale structure, phase transitions, and dynamics.

Experimental methods

Materials and sample preparation

1,10-Dibromodecane (98%), 4-bromophenol (99%), sodium sulfite (≥98%), potassium carbonate (≥99%), potassium iodide (≥99%), oxalyl chloride (≥99%), trimethylamine (>99.5%), vinylboronic acid pinacol ester (containing phenothiazine as the stabilizer, 95%), 10-bromo-1-decanol (95%), palladium(II) acetate (reagent grade, 98%), 2-dicyclohexylphosphino-2′,6′-dimethoxybiphenyl (SPhos, 98%), sodium bicarbonate ($NaHCO_3$, ACS reagent, ≥99.7%), benzyltriethylammonium bromide (99%), tripotassium phosphate trihydrate (extrapure), acetone (ACS grade), ethanol (ACS grade), 2,2′-azobis(2-methyl propionitrile) (AIBN, 98%), methanol (ACS reagent, ≥99.8%), hexanes (ACS reagent, ≥98.5%), poly(ethylene oxide) (PEO), and hydrochloric acid (ACS reagent, 37 wt%) were obtained from Sigma-Aldrich. *N*,*N*-Dimethylformamide (DMF, anhydrous, 99.8%, extra dry over molecular sieves), tetrahydrofuran (THF, anhydrous, ≥99.9%, extra dry over molecular sieves), dichloromethane (DCM, anhydrous, ≥99.8%), and acetonitrile (MeCN, anhydrous, extra dry over molecular sieves) were obtained from Thermo Scientific. Trifluoromethanesulfonamide (>98%) was purchased from TCI Chemicals. 1,4-Dioxane (99.8%, extra dry) was purchased from Acros Organics. AIBN was recrystallized from methanol, and all other materials were used as received. The snakeskin dialysis tubing with MWCO 3500 (35 mm ID) was obtained from Thermo Scientific. A Milli-Q system was used to generate deionized (DI) water (18 MΩ).

Ionomer synthesis

The synthesis and purification of LiPSC10TFSI was adapted from our previous work[25] with slight modifications, as detailed in the SI.

Preparation of PEO-ionomer blends

PEO with an average molar mass of 35 000 g mol^{-1}, was dried in a vacuum oven inside a glove box at 100 °C for 24 hours. The dried PEO was then dissolved in anhydrous acetonitrile at a concentration of 200 mg PEO per mL of acetonitrile. LiPSC10TFSI was added to PEO solution in dry vials at ethylene oxide to lithium ion (EO–Li) ratios of 2–1, 5–1, 10–1, and 20–1. After overnight stirring, the blended solutions were then drop-cast onto appropriate substrates, as detailed below for different measurements, and the solvent was completely evaporated by heating them under a vacuum oven at 120 °C for 24 hours. Removal of the solvent was confirmed with ^{1}H NMR.

NMR characterization

^{1}H NMR spectra were collected on a Bruker Avance III HD 400 Nanobay spectrometer and Bruker Avance II 800 in deuterated solvents.

Thermal characterization

The thermal properties of LiPSC10TFSI and its blends were studied using differential scanning calorimetry (DSC). A TA instrument DSC2500 was used to investigate the thermal transitions under a nitrogen purge at a flow rate of 50 mL min^{-1}. Polymer blend solutions were drop-cast into hermetic DSC pans and thoroughly dried at 120 °C for 24 hours in a vacuum oven inside the glove box. After drying, the pans were covered with lids, removed from the glove box, and immediately sealed for further testing. All samples were first heated to 250 °C and held for 1 min to erase previous thermal history. A subsequent cooling and heating cycle was applied at a ramp rate of 10 °C min^{-1} ranging from −90 °C to 250 °C with one minute isothermal holds at both temperature extremes.

X-ray scattering

Small- and Wide-Angle X-ray Scattering (SAXS/WAXS) measurements were performed at beamline 12-ID-B of the Advanced Photon Source synchrotron run by the Chemical and Materials Science Group (CMS) of the X-ray Science Division, at Argonne National Laboratory. Samples were loaded into 1.5 mm quartz capillaries (Charles Supper Company) under an argon atmosphere and sealed with epoxy. The X-ray beam had a wavelength of 0.9322 Å (corresponding to 13.3 keV), and the exposure time for each scan was 0.1 s. Scattering data were collected during cooling from 200 °C, with a 10 minute stabilization time at each measurement temperature.

Dielectric relaxation spectroscopy

Dielectric relaxation spectroscopy was performed using a Novocontrol broadband dielectric spectrometer equipped with an α-A high-performance frequency analyzer, measuring from high to low frequency in the frequency range of 0.1 Hz to 1 MHz with an AC amplitude of 0.3 V under nitrogen flow. Samples were drop-cast onto gold-coated plate electrodes, using 100 μm glass fibers as spacers to maintain consistent sample thickness. The samples were then dried at 120 °C for 24 hours in a vacuum oven inside the glove box. After drying, they were sandwiched between two gold-coated plate electrodes with a diameter of 10 mm by putting a second gold-coated electrode on top of the sample. Prior to measurements, the samples were conditioned at 200 °C between the electrodes to ensure good contact. Measurements were recorded on cooling from 200 °C to −90 °C, with a 10 min stabilization period at each temperature. The broadband dielectric spectroscopy data was fit as described in the SI.

Results and discussion

The molecular structures of the pure ionomer (LiPSC10TFSI) and the PEO are shown in Fig. 1. In the pure state, the ionomer presents lamellar nanoscale segregation of the nonpolar and ionic domains over a wide temperature range. It is anticipated that each Li^+ is coordinated by four sulfonyl oxygen groups for the pure ionomer, as in the simple salt LiTFSI the Li^+ is coordinated by four sulfonyl oxygens from four different $TFSI^-$.[29] Here, inclusion of PEO results in additional Li^+ coordination sites. The coordination of Li^+ in various electrolytes is commonly reported in the range of four to seven.[30–32] Therefore, the PEO-ionomer blend of EO–Li of 2–1 represents the case where the Li^+ must still be coordinated to the ionomer's anions while some sites could be filled by PEO. At the ratio of 5–1, sufficient PEO is present to coordinate all or most of the Li^+. Ratios of 10–1 and 20–1 have excess PEO where some polyether oxygens must remain uncoordinated. The samples were subjected to systematic investigation of their phase behavior and dynamic properties.

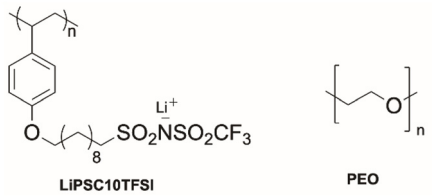

Fig. 1 Molecular structures of LiPSC10TFSI and PEO.

Calorimetry

The thermal phase transitions of the pure ionomer and its blends with PEO were investigated using DSC, as shown in Fig. 2 and Table 1 and further detailed in the SI (Table S1 and Fig. S8–S12). The pure LiPSC10TFSI showed a single glass transition temperature at 51 °C upon heating. This value was lower than that for our previously reported LiPSC10TFSI (62 °C),[25] which is likely due to decreased degree of polymerization (number average molecular weight (M_n) of 7600 g mol^{-1} estimated by end-group analysis[33,34] as described in the SI). With the addition of PEO, a notable decrease in the primary T_g was observed in all PEO-ionomer blends, which continued to decline as the PEO content increased. This behavior is consistent with the plasticizing effect of PEO on the LiPSC10TFSI ionomer matrix. PEO, with its low T_g, when mixed with the more rigid LiPSC10TFSI chains, increases the free volume and segmental mobility, leading to the decrease in the overall T_g of the PEO-ionomer blends. Interestingly, all PEO-ionomer

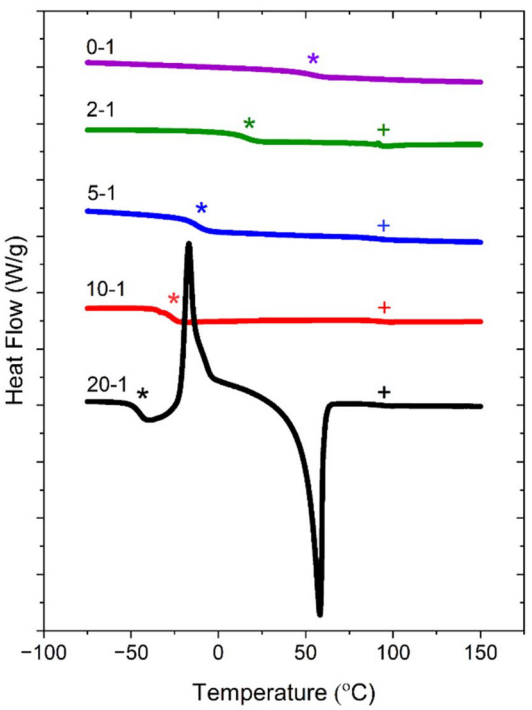

Fig. 2 Heating DSC thermograms of the pure LiPSC10TFSI and PEO-ionomer blends, with * denoting the first observed glass transition and + denoting the second, higher temperature glass transition. Curves were shifted on the y-axis for display. Complete heating and cooling DSC curves for each blend can be found in the SI.

Table 1 Table of sample compositions, density, thermal transitions, and X-ray SLD of various PEO-ionomer blends. n.d. indicates not detected

Ratio	$T_{g,1}$ (°C) DSC	$T_{g,2}$ (°C) DSC	T_m (°C) DSC	T_g (°C) DRS	Estimated density (gm cm^{-3})	Volume fraction of polar phase	X-ray SLD of the non-polar phase (10^{-6}/Å^2)	X-ray SLD of the polar phase (10^{-6}/Å^2)
0–1	51	n.d.	n.d.	56	1.22	0.26	8.36	17.99
2–1	13	90	n.d.	−14	1.21	0.38	8.36	14.84
5–1	−12	90	n.d.	−10	1.20	0.50	8.36	13.22
10–1	−30	90	n.d.	−31	1.18	0.62	8.36	12.19
20–1	−46	90	58	−34	1.17	0.75	8.36	11.54

blends, however, exhibited a more complex thermal behavior, showing a second constant T_g at 90 °C, suggesting the formation of separate, more rigid domains. Based on this calorimetry data alone, we speculated that this new T_g at higher temperature could be related to an ion-rich complex or polystyrene-backbone-rich phase.[35–38]

Furthermore, in blends with lower PEO contents (*e.g.*, 2–1, 5–1, and 10–1), no PEO crystallization and melting behavior is observed. It is important to note this absence may be a result of insufficient time for nucleation to occur in the material if the temperature ramp rate was comparatively fast. However, it is more likely the absence of crystallinity is attributed to the high concentration of lithium ions in these blends. By coordinating with the ether oxygens of PEO, these lithium ions significantly disrupt the regular packing of the PEO chains and restrict their mobility within the dense ionic network. This suppressed mobility of the PEO chains often effectively prevents them from forming organized, crystalline structures, hence the lack of distinct melting and crystallization peaks. Similar behavior is commonly reported in the literature for concentrated PEO-based electrolytes.[39–41] Lack of crystallization of the electrolyte is desirable, as crystallization is often associated with a sharp decrease in ionic conductivity.

Conversely, at higher PEO concentrations, the emergence of PEO crystallization and subsequent melting is clearly evident. For instance, the blend with an EO–Li ratio of 20–1 demonstrates a distinct PEO melting endotherm at 58 °C. Although the crystallization exotherm is not observed upon cooling, a prominent crystallization exotherm is observed during the heating scan. This classic cold crystallization peak indicates that the cooling rate was too rapid for the PEO chains to crystallize. Upon heating the sample above the glass transition temperature of the blend, sufficient thermal energy becomes available for the PEO segments to rapidly reorganize and crystallize, resulting in this large, sharp exothermic peak during the heating scan. This indicates that at high PEO concentrations, the diluting effect of excess PEO on the ionic interactions allows for chain mobility sufficient for crystallization.

Small and wide angle X-ray scattering

X-ray scattering (SAXS/WAXS) was used to investigate the effect of PEO on the structure of the pure ionomer from the atomic scale to mesoscale upon cooling. The SAXS/WAXS data for the pure ionomer previously published[22] shows a highly ordered, layered structure, characterized by sharp SAXS peaks at $q \approx 0.2$, 0.4, and 0.6 Å^{-1}. This polymeric ionic liquid crystal structure with 2-D dense ionic domains remains stable up to 180 °C.

To understand the blend morphology, SAXS/WAXS patterns for all PEO-ionomer blends were compared at 100 °C (Fig. 3). The SAXS data revealed a significant broadening and reduction in the intensity of the ionic domain-related scattering peaks as the PEO content was increased. For the 2–1 blend compared with the ionomer, the volume fraction of the polar phase was increased by ~50% and the difference in the scattering length densities (SLDs) between the polar and non-polar phases decreased by ~33% (Table 1). The intensity (I) of SAXS signal is directly proportional to the square of the difference in SLD ($I \propto (\Delta\rho)^2$), which is consistent with the decrease in signal intensity observed if considering that the PEO is homogeneously mixed with the ionic groups from the ionomer in the polar phase. Broadened SAXS peaks are clear at 0.198 and 0.383 Å^{-1}, indicating that the lamellar morphology is maintained for the 2–1 blend. For the 5–1 blend, a sole SAXS peak at 0.189 Å^{-1} is consistent with continued increase in the domain spacing due to swelling of the ionic domains with PEO. The characteristic scattering peaks in the SAXS region were further broadened for the 10–1 case but shifted to higher q (0.191 Å^{-1}) and not visible for the 20–1 case, suggesting increasing disorder. It is noted that for other PEO-based ionomeric copolymers and blends with tethered TFSI-derivative anions, the classic "ionomer peak" may not be observed due to lack of ionic aggregation and instead efficient solvation of the ionic sites by the polar polymer chains.[42,43]

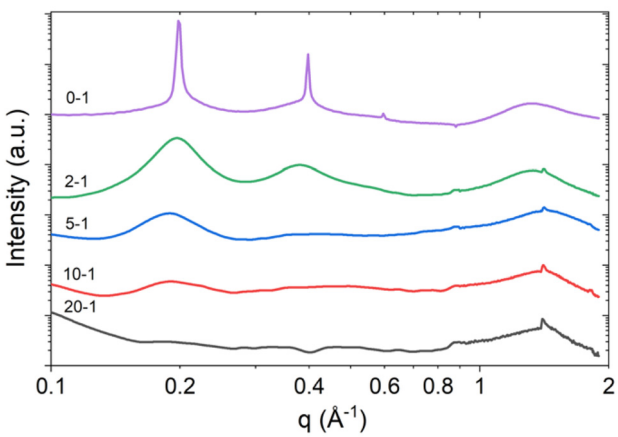

Fig. 3 SAXS/WAXS curves for pure ionomer and various PEO-ionomer blends at 100 °C.

The thermal stability of the blends was also investigated by *in situ* SAXS/WAXS measurements during cooling from 200 °C to 25 °C (Fig. S13–S16). For blends with higher PEO content, the SAXS peaks showed a more pronounced broadening at higher temperature. The peak broadening is attributed to the greater thermal mobility of PEO chains and potentially decreased dielectric constant, which disrupts the phase separation between ionic and non-polar domains. In contrast, ionomer-rich blends (*e.g.*, 2–1) exhibited a more rigid framework due to stronger ionic forces, making them less susceptible to thermal disruption. While no sharp peaks were observed in the high-q WAXS region for the 2–1, 5–1, and 10–1 blend at any temperature or for the 20–1 blends at elevated temperatures, the 20–1 blend showed significant sharp peaks at lower temperatures, confirming the crystallization of the PEO component upon cooling below its melting point.

Another notable observation from the temperature-dependent SAXS analysis was the slight increase in the q values of the SAXS peaks with increasing temperature (Table S2). This suggests that ionic interlayers in the blends become closer together at a higher temperature rather than undergoing thermal expansion. This behavior is most likely a result of stronger coulombic interactions between ions occurring at higher temperatures, as discussed in the literature.[28,44]

Finally, there are no new scattering peaks that would suggest the emergence of a new ion complex phase that produces the elevated glass transition ($T_{g,2}$) in all of the blends. Therefore, based upon this additional evidence it is hypothesized that the high temperature $T_{g,2}$ is related to the polystyrene-backbone morphology that is not visible with SAXS/WAXS.

Ionic conductivity

Dielectric spectroscopy measurements of the pure ionomer and with PEO blends were performed upon cooling, with bulk ionic conductivity values determined from the plateau value of the real part of the conductivity spectrum as depicted in Fig. 4.

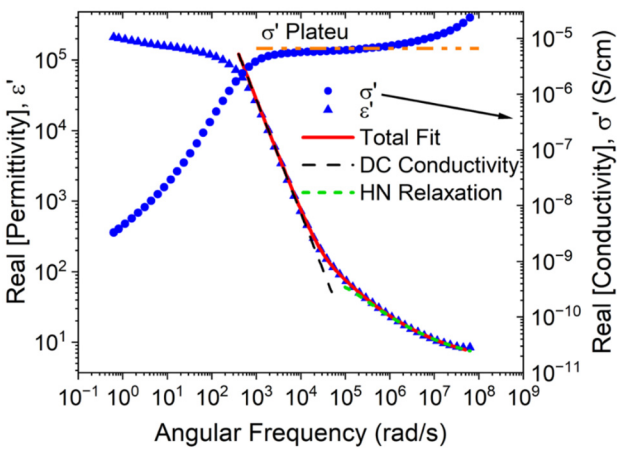

Fig. 4 Real component of the permittivity (left y-axis) of 5–1 PEO-ionomer at 90 °C with fits of the individual components and total fit, along with the real component of the conductivity (right y-axis).

The temperature dependence of these conductivities is presented in Fig. 5. The pure side-chain ionomer and blends at ratios of 2–1, 5–1, and 10–1 consistently exhibit Vogel–Fulcher–Thammann (VFT) temperature dependencies across the measured range, consistent with long-range ion transport being coupled to matrix relaxation. In contrast, the temperature dependency of ionic conductivity of 20–1 blend shows the VFT behavior at higher temperatures (200 °C to 45 °C) but shows Arrhenius behavior at lower temperatures due to crystallization of some of the PEO.

At 90 °C, the ionic conductivity of the PEO-ionomer blends exhibits a clear trend of increasing conductivity with higher PEO content (Table 2). A modest increase in conductivity at lower temperatures is observed when introducing the 2–1 EO–Li ratio blend compared to the pure ionomer. However, a significant enhancement in conductivity is evident as the PEO content increases further, with the 5–1 blend showing an approximate 2.3 orders of magnitude increase in conductivity compared to the 2–1 blend. This substantial jump in conductivity for the 5–1 blend is primarily attributed to the establishment of an optimal coordination environment for the lithium ions by the ether oxygens of PEO, which significantly enhances ion mobility in this composition. In the 2–1 blend, there is an insufficient amount of PEO to achieve complete and efficient coordination of all lithium ions, leading to increased ion-ion interaction. Conversely, the 5–1 blend provides sufficient ether oxygens from PEO to optimally coordinate the lithium ions, which significantly enhances their dissociation and mobility.

While this upward trend in conductivity continues for the 10–1 and 20–1 blends, the observed increases are again modest in these higher PEO content blends. This plateauing of the conductivity enhancement suggests that beyond the 5–1 ratio, the additional PEO might not significantly contribute to

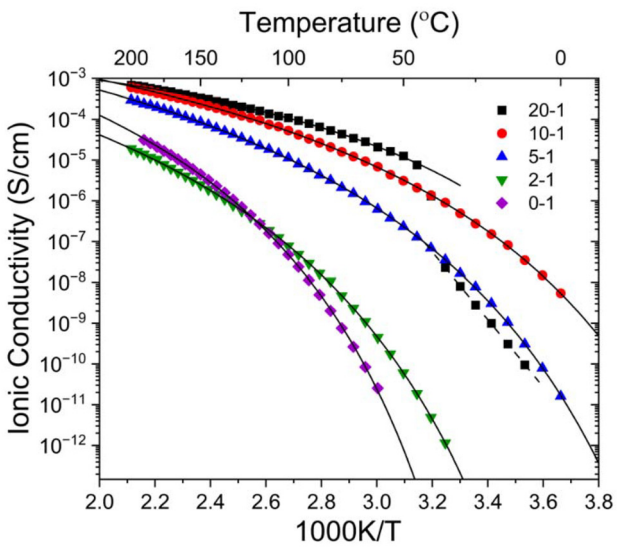

Fig. 5 Ionic conductivity of pure ionomer and PEO-ionomer blends with respect to inverse temperature, along with VFT (solid lines) and Arrhenius (dotted line) fits.

Table 2 Conductivity of various solid polymer electrolytes in this work and others

Material	Temperature (°C)	Conductivity (S cm^{-1})	Reference
PEO-ionomer (20–1)	90	7.9×10^{-5}	This work
PEO-ionomer (10–1)	90	3.3×10^{-5}	This work
PEO-ionomer (5–1)	90	6.1×10^{-6}	This work
PEO-ionomer (2–1)	90	2.9×10^{-8}	This work
Pure ionomer (0–1)	90	1.1×10^{-8}	This work
PEO-p5PhTFSI-Li (7.7–1)	90	2.0×10^{-4}	Nguyen, Nam, *et al.*[45]
PEO-p5PhTFSI-Li (10–1)	90	3.8×10^{-5}	Paren, Benjamin A., *et al.*[28]
PEO-(polyFAST-NO)	80	6.6×10^{-5}	Zhang, Wenxu *et al.*[47]
PEO-LiPSS (20–1)	90	1.9×10^{-7}	Ma, Qiang, *et al.*[48]
PEO-LiPSTFSI (20–1)	90	3.2×10^{-5}	
PEO-LiPSsTFSI (20–1)	90	1.5×10^{-4}	
PEO-LiTFSI (20–1)	90	1.3×10^{-3}	
PEO-LiPSFSI (20–1)	90	3.9×10^{-5}	Ma, Qiang, *et al.*[46]

further lithium-ion coordination, as the optimal coordination sphere may already be established. Instead, the excess PEO might primarily contribute to increasing the relaxation rate in the polar phase which will be discussed in the later sections. The 20–1 blend demonstrates a conductivity of approximately 4 orders of magnitude greater than that of the pure ionomer (0–1) at 90 °C.

Table 2 compares the ionic conductivity of the PEO-ionomer blends investigated in this work with a selection of previously reported solid polymer electrolytes. The data presented at a consistent temperature of 90 °C (unless otherwise specified) to allow a direct comparison of performance. As shown in Table 2, the PEO-ionomer blend (20–1) exhibits an ionic conductivity of 7.9×10^{-5} S cm^{-1} at 90 °C. This result is similar to other advanced single-ion conducting polymer electrolytes reported in the literature, such as the PEO-p5PhTFSI-Li (3.8×10^{-5} S cm^{-1} and 2.0×10^{-4}, with varied PEO molecular weights and loadings),[28,45] PEO-LiPSFSI (3.9×10^{-5} S cm^{-1}),[46] and a PEO-(polyFAST-NO) blend (6.6×10^{-5} S cm^{-1} at 80 °C).[47] The performance of the aforementioned blends is notably superior to that of systems like PEO-LiPSS (1.9×10^{-7} S cm^{-1}),[48] which have a less delocalized sulfonate anion directly tethered to the polymer backbone.

While most of the ionomers reported here tether their ionic group directly to the polymer backbone, our unique ionomer consists of a polystyrene backbone with a flexible decyl side chain. The bulky, charge delocalized TFSI anion is tethered to the side chain rather than directly into the backbone. This design enhances the flexibility and mobility of the tethered anion, which contributes to increased segmental relaxation and facilitates more efficient lithium-ion transport in the pure ionomer case.[49] However, it is seen here that the hydrophobic side-chain does not result in improved conductivity for the PEO-ionomer blends, which is likely because the non-polar side-chain does not promote mixing between the PEO and the tethered ionic group.

Dielectric relaxation and ion transport analyses

The broadband dielectric spectroscopy data was fit to an equation containing a power law term for the electrode polarization and a single Havriliak–Negami relaxation term, as described below in eqn (1).[25,28,36] The same procedure and equation was found to result in adequate fit for all samples, despite the substantial difference in the bulk ionic conductivity between the samples and the fact that the blends contain multiple polar groups that can contribute to the dielectric relaxation.

$$\varepsilon^* = \varepsilon' - i\varepsilon'' = A\omega^{-n} + \frac{i\sigma}{\varepsilon_0\omega} + \varepsilon_\infty + \frac{\Delta\varepsilon}{[1 + (i\omega\tau_{HN})^a]^b} \quad (1)$$

Here, ε^* represents the complex permittivity, ε' is the real permittivity, ε'' is the imaginary permittivity, A is the power law prefactor, n is the power of the power law, σ is the DC conductivity, ε_0 is the permittivity of free space, ε_∞ is the permittivity at infinite frequency, τ_{HN} is the relaxation time associated with the Havriliak–Negami relaxation, $\Delta\varepsilon$ is the strength of relaxation, and a and b are shape parameters.

The static dielectric constant (ε_s), of the pure ionomer and blends was obtained by summing $\Delta\varepsilon$ and ε_∞ from Havriliak–Negami model fitting ($\Delta\varepsilon = \varepsilon_s - \varepsilon_\infty$) and is shown in Fig. 6. In the pure ionomer (0–1), and blends 2–1 and 5–1, it is observed that ε_s increases with increasing temperature, unlike Onsager predictions where ε_s decreases as the temperature increases.[50,51] In ionomer-based materials, this temperature-dependent increase in ε_s is due to the greater movement and rearrangement of ions at higher temperatures. This effect is

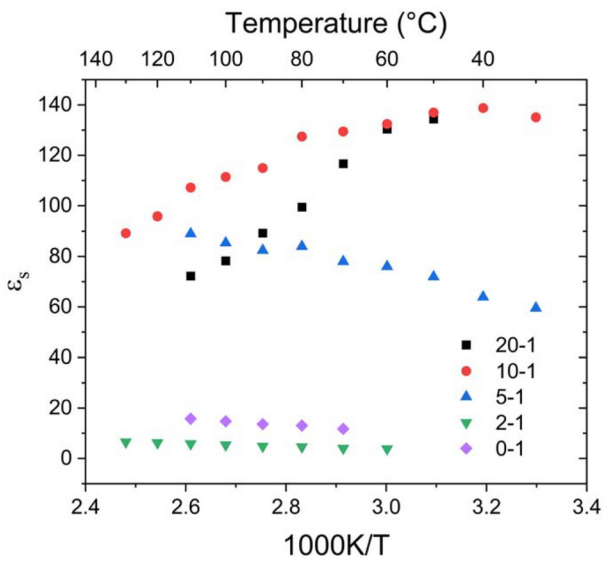

Fig. 6 Dielectric constants, ε_s, for pure ionomer and various PEO-ionomer blends as a function of inverse temperature.

particularly relevant in systems exhibiting phase-separated structures having highly concentrated ionic domains.[50,51]

Consistent with the previous studies on PEO-ionomer blends,[28] the ε_s of the pure ionomer (0–1) was found slightly higher than that of the 2–1 blend, even though pure ionomer has more dense ionic domains and ordered structure. In the 2–1 blend there is not enough PEO to fully solvate the lithium cations, so there must still be significant ion pairing. The 2–1 blend also exhibits less ordered domains than the pure ionomer, which we hypothesize could potentially result in a lower dielectric constant. The PEO may act as a crosslinker, coordinating to lithium cations that individually coordinate with anions attached to side-chains in different non-polar domains and resulting in less local anion alignment. The drastic enhancement in the ε_s values of 5–1 in comparison to 2–1 is likely due to ionic domains being swollen by enough PEO to significantly enhance the lithium ions dissociation from the tethered anions and their long-range rearrangement within dynamically forming ionic networks.

However, in the blends with higher PEO content (10–1 and 20–1), the ε_s decreases with increasing temperature, although these blends exhibit higher ε_s value compared to other blends. This higher magnitude of ε_s results from the strong dissociation of ions facilitated by the high PEO content, which effectively dilutes the ionomer's ionic domains, thereby reducing ion aggregation and allowing dipoles to respond more freely to an applied electric field. The observed decrease in ε_s with increasing temperature is consistent with predictions from the Onsager theory for polar liquids, a behavior commonly observed in ionomers and ionomer-polymer blends.[28,50,52,53] According to this model, reduced thermal energy at lower temperatures allows for a more effective alignment of permanent dipoles with the electric field, thus enhancing macroscopic polarization and, consequently ε_s.

To probe the dielectric relaxation behavior, maximum angular frequency (ω_{max}), or dielectric relaxation rate are calculated by parameters gained from H–N model fitting, as shown in eqn (2).

$$\frac{1}{\omega_{max}} = \tau_{max} = \tau_{HN}\left(\sin\frac{ab\pi}{2+2b}\right)^{\frac{1}{a}}\left(\sin\frac{a\pi}{2+2b}\right)^{-\frac{1}{a}} \quad (2)$$

The temperature dependence of the maximum dielectric relaxation rate (ω_{max}) for all investigated samples, including the pure ionomer and the PEO-ionomer blends, follows VFT behavior (shown in Fig. 7), suggesting that the dielectric process is coupled to conductivity relaxation and originates from free volume. Extrapolating the VFT fitting curve to an angular frequency of 0.01 rad s^{-1} allows for the determination of the dielectric relaxation spectroscopy glass transition temperature (DRS T_g). This specific angular frequency represents the condition where the material's structure is effectively frozen. The DRS T_g for pure ionomer is 56 °C, substantially higher than the DRS T_g's of −14, −10, −31, and −34 °C for 2–1, 5–1, 10–1, and 20–1 PEO-ionomer blends. These T_g values obtained from DSC and DRS experiments are within 15 °C for all pure ionomer and 5–1, 10–1, and 20–1 PEO-ionomer blends suggesting that dielectric relaxation processes in these blends are highly correlated with segmental relaxation, with probably some amount of relaxation from the local ion rearrangement as well. However, the 2–1 PEO-ionomer blend exhibits a relatively higher difference between its DSC and DRS T_g values than other blends. This is likely due to the small amount of PEO acting as a crosslinker, which slows the large-scale polymer motion relative to the higher PEO content cases while still allowing for more localized ion hopping relative to the pure ionomer case to be measured by DRS.

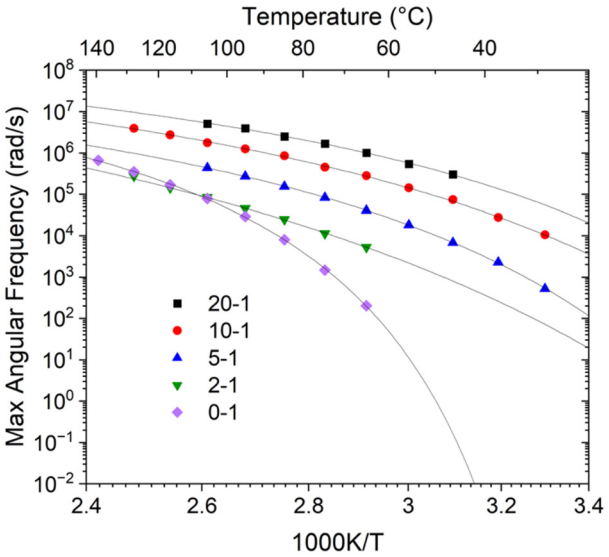

Fig. 7 Maximum dielectric relaxation rates, ω_{max}, for pure ionomer and various PEO-ionomer blends plotted as functions of inverse temperature, along with lines representing VFT fits.

While the relaxation rate of pure ionomer at higher temperatures is comparable to, or even slightly higher than, that of the most concentrated PEO blend (2–1 EO–Li), its ω_{max} decreases much faster than those of all other PEO-ionomer blends as temperature decreases. In contrast, for the PEO-ionomer blends (2–1 to 20–1 EO–Li), the relaxation rate shows a clear trend: it gradually increases with increasing PEO concentration of the blend. This suggests that the decreased ion density in the ionic domain leads to enhanced conductivity relaxation. This dynamic behavior is somewhat aligned with the observed ionic conductivities of the pure ionomer and the PEO-ionomer blends, as presented in Fig. 5, except that the jump in bulk ionic conductivity between the 2–1 and 5–1 PEO-ionomer blends substantially exceeds the jump in the conductivity relaxation rate.

To further interrogate the ion transport mechanism, the ionic conductivity is presented against normalized temperature by DSC $T_{g,1}$ and DRS T_g respectively. The degree to which these normalized conductivity curves overlap across different samples directly indicates whether the DC conduction mechanism is similarly governed by the respective glass transition (DSC or DRS) for all compositions.

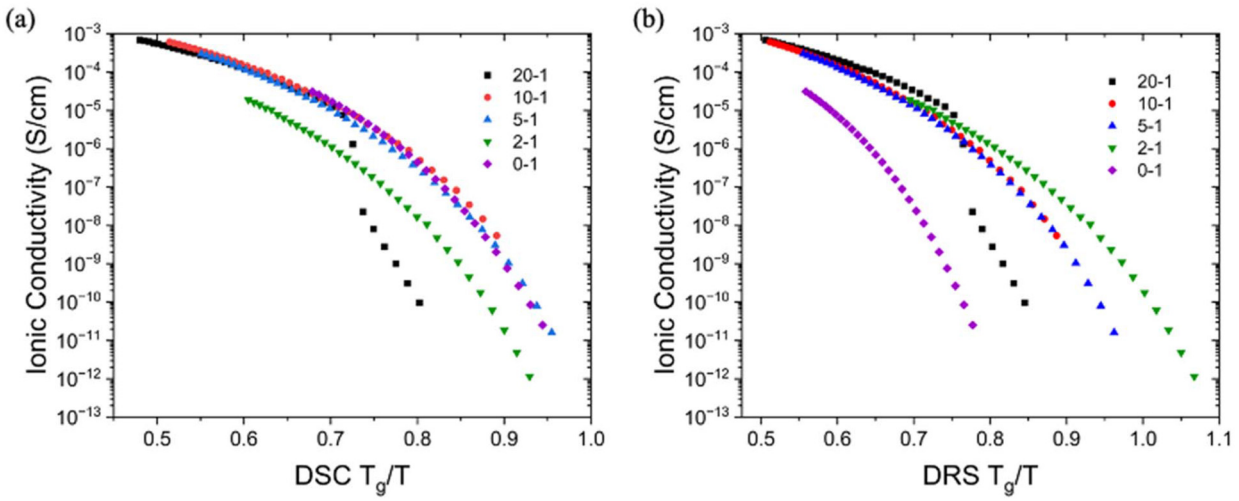

Fig. 8 Ionic conductivity of pure ionomer and PEO-ionomer blends plotted against normalized temperature using glass transition temperatures obtained from (a) DSC heating data and (b) DRS VFT extrapolation.

As shown in Fig. 8a, the DSC $T_{g,1}$ normalized conductivity of pure ionomer (0–1), 5–1, and 10–1 PEO-ionomer blends are very close to each other across the entire investigated temperature range. This overlap indicates that for all these compositions, the primary mechanism of ion transport is consistently coupled to the polymer's segmental dynamics, with the DSC glass transition temperature effectively normalizing their conductivity behavior. The significant drop in the DSC $T_{g,1}$-normalized conductivity curve for the 2–1 blend, suggests decoupling between ion movement and polymer segmental dynamics for this specific composition. The significant drop in DSC $T_{g,1}$ between the pure ionomer and 2–1 blend does not increase the real ionic conductivity. This result may be due to the dilute PEO acting as a crosslinker between ions connected to side-chains from different non-polar domains and slowing their long-range motion. Conversely, while the 20–1 blend's DSC $T_{g,1}$-normalized conductivity initially aligns with the master curve at higher temperatures, it drops sharply at lower temperatures due to crystallization.

A more nuanced understanding of the ion transport mechanism emerges from the DRS T_g-normalized conductivity curves, as shown in Fig. 8b. Here the pure ionomer's curve deviates significantly from the other PEO-ionomer blends. This highlights a different influence of the dielectric relaxation process between the blends in the melt state and the pure ionomer, across the entire investigated blend composition range of 2–1 to 20–1. This suggests that the bulk ionic conductivity, or long-range ion motion, in the pure ionomer is restricted by the dense ionic aggregation. In the pure ionomer, a smaller fraction of the local ion motions may be contributing to long-range ion transport; backward ion motion may be more prevalent.[54] In contrast, the 2–1, 5–1, 10–1, and 20–1 blends in the melt state remain comparatively close in the DRS T_g-normalized conductivity plot, indicating the role of PEO in facilitating long-range ion transport that is coupled to the dielectric relaxation.

Barton, Nakajima, and Namikawa (BNN) have proposed a linear scaling theory between ionic conductivity and the dielectric relaxation rate.[1,55,56] The BNN plot relation is empirically described by $\sigma = B\varepsilon_0\omega_{max}$. As shown in the BNN plot (Fig. 9), the observed behavior of materials varies significantly. The pure ionomer exhibits a scaling factor B value falling slightly below the ideal scaling line (i = 1), indicating that the ion rearrangement process governs the lithium ions transport. In contrast, all the PEO-ionomer blends show that their data points lie above the ideal scaling line. The 20–1 blend in the melt state shows a distinctly higher B, which indicates that when accounting for differences in the conductivity relaxation and dielectric constant that the long-range ion motion is faster for this sample and distinct from the other blends. These results are in agreement with substantial research literature

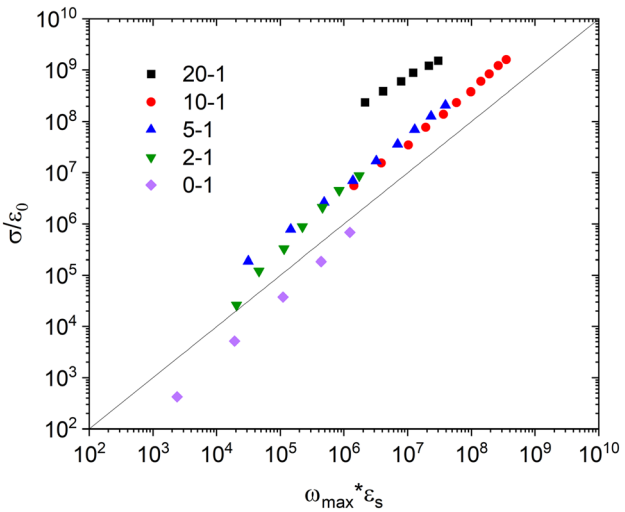

Fig. 9 BNN scaling plot for pure ionomer and PEO-ionomer blends. The line represents the ideal scaling factor, B = 1.

showing that bulk lithium-ion conductivity in single-ion conductors containing PEO is optimized when ion contents are in the range of EO–Li of 20–1 to 30–1, due to decreased ionic aggregation and increased segmental relaxation compared to higher ion concentration cases.

Conclusions

Polymer electrolyte blends of a liquid crystalline ionomer (LiPSC10TFSI) were prepared with PEO at varying ethylene oxide (EO) to lithium (Li) ratios. A combination of techniques was used to investigate the thermal properties, morphology, and ion transport characteristics of these PEO-ionomer blends. The addition of PEO to the ionomer caused a reduction in the primary glass transition temperature with the emergence of a new glass transition that is anticipated to be related to the polystyrene-backbone of the ionomer. Upon the addition of small amounts of PEO at a 2–1 ratio, the lamellar morphology of the side-chain ionomer appeared to be maintained. At higher blend ratios, increasing disorder appears to occur. PEO inclusion substantially enhanced ionic conductivities of the blends relative to the pure ionomer, with the 20–1 blend achieving 7.9×10^{-5} S cm^{-1} at 90° C which is around 4 orders of magnitude greater than that of pure ionomer. A significant jump in conductivity (2.3 order of magnitude) occurred from 2–1 to 5–1, likely due to an optimal coordination environment for the lithium ions by the ether oxygen of PEO, which significantly enhances mobility. However, conductivities for 10–1 and 20–1 blends show only modest further increase, suggesting a saturation of lithium coordination effects. Dielectric relaxation spectroscopy indicated that the long-range ion transport is generally coupled to dielectric relaxation across the blends, while conductivity normalization and the BNN plot indicating some differences in conduction mechanisms with varying PEO content. The data suggests that inclusion of PEO increases the coupling between dielectric relaxation and long-range ion transport.

Author contributions

Govind Prasad Devkota: writing – original draft, writing – review & editing, methodology, investigation, visualization, formal analysis, data curation. Carter K. Dauenhauer: writing – original draft, formal analysis, data curation, visualization. Jizhou Jiang: formal analysis, visualization. Jennifer L. Schaefer: writing – review & editing, supervision, project administration, funding acquisition, methodology, conceptualization.

Conflicts of interest

The authors declare no other conflicts of interest.

Data availability

Detailed synthetic procedures, NMR spectra, description of the end-group analysis, DSC plots and tabulated phase transition data, temperature-dependent SAXS/WAXS plots and tabulated primary peak positions and associated analysis impacting the estimated SLDs, dielectric fitting procedures used, and a plot of dielectric relaxation times have been included as a part of the supplementary information (SI). See DOI: https://doi.org/10.1039/d5py00769k.

Raw data may be provided by the authors upon request.

Acknowledgements

The authors thank the University of Notre Dame for the primary financial support for this study. We also thank the National Science Foundation for prior support *via* DMR-1654162 for the preceding research on this material system and for supplies that we used to continue this current research study. The authors also acknowledge Dr Benajamin A. Paren at Stevens Institute of Technology for assistance with dielectric relaxation spectroscopy fitting; Dr Xiaobing Zuo at Advanced Photon Source beamline 12-ID-B at Argonne National Laboratory for assistance with X-ray scattering; the University of Notre Dame Magnetic Resonance Research Center for NMR instrumentation; and the University of Notre Dame Center for Environmental Science and Technology (CEST) for ICP-OES instrumentation. This research was performed on APS beam time award (https://doi.org/10.46936/APS-189946/60014059) from the Advanced Photon source, a U. S. Department of energy (DOE) Office of Science user facility operated for the DOE Office of Science by Argonne National Laboratory under Contract No. DE-AC02-06CH11357.

References

1 J. R. Macdonald, *J. Appl. Phys.*, 2010, **107**, 101101.
2 J. F. Pierdoná Antoniolli, G. L. Grespan and D. Rodrigues, *ChemSusChem*, 2024, **17**, e202301808.
3 H. Zhang, C. Li, M. Piszcz, E. Coya, T. Rojo, L. M. Rodriguez-Martinez, M. Armand and Z. Zhou, *Chem. Soc. Rev.*, 2017, **46**, 797–815.
4 A. Manthiram, X. Yu and S. Wang, *Nat. Rev. Mater.*, 2017, **2**, 16013.
5 Z. Xue, D. He and X. Xie, *J. Mater. Chem. A*, 2015, **3**, 19218–19253.
6 D. Zhou, D. Shanmukaraj, A. Tkacheva, M. Armand and G. Wang, *Chem*, 2019, **5**, 2326–2352.
7 J. Tan, L. Guo, J. Hu and S. Liu, *J. Phys. Chem. C*, 2024, **128**, 17197–17218.
8 J. Mu, S. Liao, L. Shi, B. Su, F. Xu, Z. Guo, H. Li and F. Wei, *Polym. Chem.*, 2024, **15**, 473–499.
9 J. Gao, C. Wang, D.-W. Han and D.-M. Shin, *Chem. Sci.*, 2021, **12**, 13248–13272.

10 X. Shan, Z. Song, H. Ding, L. Li, Y. Tian, A. P. Sokolov, M. Tian, K. Xu and P.-F. Cao, *Energy Environ. Sci.*, 2024, **17**, 8457–8481.
11 X. Shan, S. Zhao, M. Ma, Y. Pan, Z. Xiao, B. Li, A. P. Sokolov, M. Tian, H. Yang and P.-F. Cao, *ACS Appl. Mater. Interfaces*, 2022, **14**, 56110–56119.
12 X. Zhang, A. Wang, X. Liu and J. Luo, *Acc. Chem. Res.*, 2019, **52**, 3223–3232.
13 D. J. Brooks, B. V. Merinov, W. A. Goddard, B. Kozinsky and J. Mailoa, *Macromolecules*, 2018, **51**, 8987–8995.
14 B. Sun, J. Mindemark, E. V. Morozov, L. T. Costa, M. Bergman, P. Johansson, Y. Fang, I. Furó and D. Brandell, *Phys. Chem. Chem. Phys.*, 2016, **18**, 9504–9513.
15 J. Chen, Q. Liu, Z. Shen, X. Peng, J. Bian, Z. Bao, Y. Chen and S. Bi, *Mater. Lett.*, 2025, **398**, 138882.
16 Y. Lin, C. Heng, Y. Liu, Y. Xu, T. Wen, A. Facchetti and L. Ding, *Langmuir*, 2025, **41**, 17875–17884.
17 M. Zhang, C. Lei, T. Zhou, S. Song, P. Paoprasert, X. He and X. Liang, *ACS Appl. Mater. Interfaces*, 2022, **14**, 55653–55663.
18 X. C. Chen, R. L. Sacci, N. C. Osti, M. Tyagi, Y. Wang, J. K. Keum and N. J. Dudney, *Front. Chem.*, 2021, **8**, 592604.
19 L. Yan, L. Hoang and K. I. Winey, *Macromolecules*, 2020, **53**, 1777–1784.
20 L. M. Hall, M. E. Seitz, K. I. Winey, K. L. Opper, K. B. Wagener, M. J. Stevens and A. L. Frischknecht, *J. Am. Chem. Soc.*, 2012, **134**, 574–587.
21 L. Yan, M. Häußler, J. Bauer, S. Mecking and K. I. Winey, *Macromolecules*, 2019, **52**, 4949–4956.
22 C. Rank, L. Yan, S. Mecking and K. I. Winey, *Macromolecules*, 2019, **52**, 8466–8475.
23 J. Liu, P. D. Pickett, B. Park, S. P. Upadhyay, S. V. Orski and J. L. Schaefer, *Polym. Chem.*, 2020, **11**, 461–471.
24 J. Liu, L. Yang, P. D. Pickett, B. Park and J. L. Schaefer, *Macromolecules*, 2022, **55**, 7752–7762.
25 J. Liu and J. L. Schaefer, *Macromolecules*, 2023, **56**, 2515–2525.
26 R. Meziane, J.-P. Bonnet, M. Courty, K. Djellab and M. Armand, *Electrochim. Acta*, 2011, **57**, 14–19.
27 S. Zhao, H. Che, S. Chen, H. Tao, J. Liao, X.-Z. Liao and Z.-F. Ma, *Electrochem. Energy Rev.*, 2024, **7**, 3.
28 B. A. Paren, N. Nguyen, V. Ballance, D. T. Hallinan, J. G. Kennemur and K. I. Winey, *Macromolecules*, 2022, **55**, 4692–4702.
29 J. L. Nowinski, P. Lightfoot and P. G. Bruce, *J. Mater. Chem.*, 1994, **4**, 1579–1580.
30 O. Borodin, G. D. Smith and W. Henderson, *J. Phys. Chem. B*, 2006, **110**, 16879–16886.
31 K. Yuan, H. Bian, Y. Shen, B. Jiang, J. Li, Y. Zhang, H. Chen and J. Zheng, *J. Phys. Chem. B*, 2014, **118**, 3121–3126.
32 N. Molinari, J. P. Mailoa and B. Kozinsky, *Chem. Mater.*, 2018, **30**, 6298–6306.
33 J. C. Bevington, B. J. Hunt and C. A. Barson, *Macromol. Symp.*, 1996, **111**, 293–303.
34 J. C. Bevington and T. N. Huckerby, *Eur. Polym. J.*, 2006, **42**, 1433–1436.
35 C. Appiah, J. Akbarzadeh, H. Peterlik and W. H. Binder, *Eur. Polym. J.*, 2015, **64**, 138–146.
36 F. Fan, Y. Wang and A. P. Sokolov, *Macromolecules*, 2013, **46**, 9380–9389.
37 W. Brostow, R. Chiu, I. M. Kalogeras and A. Vassilikou-Dova, *Mater. Lett.*, 2008, **62**, 3152–3155.
38 A. N. Gaikwad, E. R. Wood, T. Ngai and T. P. Lodge, *Macromolecules*, 2008, **41**, 2502–2508.
39 M. Marzantowicz, J. R. Dygas, F. Krok, A. Łasińska, Z. Florjańczyk, E. Zygadło-Monikowska and A. Affek, *Electrochim. Acta*, 2005, **50**, 3969–3977.
40 W.-S. Young, J. N. L. Albert, A. B. Schantz and T. H. Epps, *Macromolecules*, 2011, **44**, 8116–8123.
41 B. Kumar, S. J. Rodrigues and S. Koka, *Electrochim. Acta*, 2002, **47**, 4125–4131.
42 C. T. Elmore, M. E. Seidler, H. O. Ford, L. C. Merrill, S. P. Upadhyay, W. F. Schneider and J. L. Schaefer, *Batteries*, 2018, **4**, 28.
43 X. Chen, F. Chen, M. S. Liu and M. Forsyth, *Solid State Ionics*, 2016, **288**, 271–276.
44 W. Wang, G. J. Tudryn, R. H. Colby and K. I. Winey, *J. Am. Chem. Soc.*, 2011, **133**, 10826–10831.
45 N. Nguyen, M. P. Blatt, K. Kim, D. T. Hallinan and J. G. Kennemur, *Polym. Chem.*, 2022, **13**, 4309–4323.
46 Q. Ma, Y. Xia, W. Feng, J. Nie, Y.-S. Hu, H. Li, X. Huang, L. Chen, M. Armand and Z. Zhou, *RSC Adv.*, 2016, **6**, 32454–32461.
47 W. Zhang, S. Feng, M. Huang, B. Qiao, K. Shigenobu, L. Giordano, J. Lopez, R. Tatara, K. Ueno, K. Dokko, M. Watanabe, Y. Shao-Horn and J. A. Johnson, *Chem. Mater.*, 2021, **33**, 524–534.
48 Q. Ma, H. Zhang, C. Zhou, L. Zheng, P. Cheng, J. Nie, W. Feng, Y. Hu, H. Li, X. Huang, L. Chen, M. Armand and Z. Zhou, *Angew. Chem., Int. Ed.*, 2016, **55**, 2521–2525.
49 J. Liu, M. Diaz-Segura, A. S. Manning, L. Yang, G. Devkota, S. P. Upadhyay, J. K. Whitmer and J. L. Schaefer, *Electrochim. Acta*, 2025, **511**, 145415.
50 U. H. Choi, M. Lee, S. Wang, W. Liu, K. I. Winey, H. W. Gibson and R. H. Colby, *Macromolecules*, 2012, **45**, 3974–3985.
51 U. H. Choi, A. Mittal, T. L. Price, H. W. Gibson, J. Runt and R. H. Colby, *Macromolecules*, 2013, **46**, 1175–1186.
52 W. Wang, G. J. Tudryn, R. H. Colby and K. I. Winey, *J. Am. Chem. Soc.*, 2011, **133**, 10826–10831.
53 L. Onsager.
54 E. W. Stacy, C. P. Gainaru, M. Gobet, Z. Wojnarowska, V. Bocharova, S. G. Greenbaum and A. P. Sokolov, *Macromolecules*, 2018, **51**, 8637–8645.
55 H. Namikawa, *J. Non-Cryst. Solids*, 1975, **18**, 173–195.
56 H. Namikawa, *J. Non-Cryst. Solids*, 1974, **14**, 88–100.